Topological magnetotransport and electrical switching of sputtered antiferromagnetic $Ir_{20}Mn_{80}$

Danrong Xiong(熊丹荣)[1,2], Yuhao Jiang(蒋宇昊)[1], Daoqian Zhu(朱道乾)[1], Ao Du(杜奥)[1], Zongxia Guo(郭宗夏)[1], Shiyang Lu(卢世阳)[3], Chunxu Wang(王春旭)[3], Qingtao Xia(夏清涛)[3], Dapeng Zhu(朱大鹏)[1,3,†], and Weisheng Zhao(赵巍胜)[1,2,3,‡]

[1] *Fert Beijing Institute, MIIT Key Laboratory of Spintronics, School of Integrated Circuit Science and Engineering, Beihang University, Beijing* 100191, *China*

[2] *Hefei Innovation Research Institute, Beihang University, Hefei* 230013, *China*

[3] *Beihang–Goertek Joint Microelectronics Institute, Qingdao Research Institute, Beihang University, Qingdao* 266000, *China*

(Received 27 November 2022; revised manuscript received 19 January 2023; accepted manuscript online 8 February 2023)

Topological magnetotransport in non-collinear antiferromagnets has attracted extensive attention due to the exotic phenomena such as large anomalous Hall effect (AHE), magnetic spin Hall effect, and chiral anomaly. The materials exhibiting topological antiferromagnetic physics are typically limited in special Mn_3X family such as Mn_3Sn and Mn_3Ge. Exploring the topological magnetotransport in common antiferromagnetic materials widely used in spintronics will not only enrich the platforms for investigating the non-collinear antiferromagnetic physics, but also have great importance for driving the nontrivial topological properties towards practical applications. Here, we report remarkable AHE, anisotropic and negative parallel magnetoresistance in the magnetron-sputtered $Ir_{20}Mn_{80}$ antiferromagnet, which is one of the most widely used antiferromagnetic materials in industrial spintronics. The *ab initio* calculations suggest that the Ir_4Mn_{16} ($IrMn_4$) or Mn_3Ir nanocrystals hold nontrivial electronic band structures, which may contribute to the observed intriguing magnetotransport properties in the $Ir_{20}Mn_{80}$. Further, we demonstrate the spin–orbit torque switching of the antiferromagnetic $Ir_{20}Mn_{80}$ by the spin Hall current of Pt. The presented results highlight a great potential of the magnetron-sputtered $Ir_{20}Mn_{80}$ film for exploring the topological antiferromagnet-based physics and spintronics applications.

Keywords: non-collinear antiferromagnets, anomalous Hall effect, magnetization switching, spin–orbit torque

PACS: 75.47.–m, 85.75.–d, 71.70.Ej **DOI:** 10.1088/1674-1056/acb9ec

1. Introduction

Antiferromagnets (AFMs) are promising for replacing ferromagnets as active elements in future spintronics devices owing to their absence of magnetic stray fields, immunity to external magnetic fields, and intrinsic dynamics in the terahertz range.[1–11] In particular, non-collinear AFMs such as Mn_3X (X = Sn, Ge, Ir, or Pt) with a broken time-reversal symmetry have recently attracted extensive research attentions due to their nontrivial electronic band structures.[12–16] For instance, the non-vanishing Berry curvature of topological Bloch bands induces a large anomalous Hall effect (AHE) despite the zero or negligibly small net magnetization in the non-collinear AFMs, which provides a good platform for exploring the intrinsic AHE physics and a convenient way to access the magnetic states in AFMs.[17–19] Also, theoretical and experimental studies have demonstrated that non-collinear AFMs possess singularities in the momentum space with broken time-reversal symmetry, *i.e.*, Weyl points, which supports for pursuing the quantum quasiparticles of Weyl fermions.[13,20–23] The abundant intriguing properties of non-collinear AFMs have advanced much the antiferromagnetic spintronics, but the reported materials so far are limited in a few Mn_3X single crystalline or polycrystalline films,[23,24] and the Cr film with local spin frustration.[25] Exploring the topological magnetotransport in AFM materials widely used in industrial spintronics will not only provide new platforms for investigating the noncollinear AFM physics, but also is of great importance to drive the researches of the nontrivial topological properties towards practical applications.

On the other hand, efficient electrical writing and reading information that is stored via AFM Néel vector is of great significance for exploring the antiferromagnetic memory and logic devices.[1,3,6] Towards electrical writing of the AFM order, a few works have reported that in AFMs with broken inversion symmetry such as the CuMnAs[26–28] and Mn_2Au,[29–31] the intrinsic Néel spin–orbit torques (SOTs) originating from the inverse spin galvanic effect can efficiently drive the Néel vector switching.[32,33] The later studies in the AFM insulators such as NiO,[34–36] CoO,[37] and Fe_2O_3[38–40] interfaced with a heavy metal (HM) have also evidenced the electrical Néel order switching, with the driving mechanism of SOT or thermo-related magnetic effects.[41,42] Recently, electrical switching of non-collinear AFMs have also been demonstrated.[22,43–45] These electrically switched AFMs are either special materials with certain crystalline sym-

†Corresponding author. E-mail: zhudp@buaa.edu.cn
‡Corresponding author. E-mail: weisheng.zhao@buaa.edu.cn

© 2023 Chinese Physical Society and IOP Publishing Ltd

metry and magnetic atoms occupation, or dielectric films with complex coupling between the thermal, elastic, and magnetic effects,[42] The realization of electrical switching of Néel order in common AFM materials is highly desired for applications,[46] following which a few recent works have reported the electrical switching of common metallic AFMs such as PtMn.[46,47]

IrMn, a binary metallic alloy, is one of the most widely used AFM materials as pining layer to adjacent ferromagnet for magnetic sensor and magnetic random access memory devices in industrial spintronics.[48] As compared with other collinear or non-collinear metallic AFMs such as FeMn, PtMn, Mn_3Sn, and Mn_3Ge, the IrMn has the thinnest thickness to retain the AFM phase,[49–51] and maintains the antiferromagnetic phase for a considerable stoichiometric range.[52] And compared with other different Ir and Mn atomic ratios, the $Ir_{20}Mn_{80}$ exhibits the maximum exchange coupling strength,[53] the highest blocking temperature,[53] together with strongest (111) texture,[54] and thus is of technological importance.[55] In this work, we experimentally show remarkable AHE in the magnetron-sputtered antiferromagnetic $Ir_{20}Mn_{80}$ thin film. The *ab initio* calculations suggest the Ir_4Mn_{16} ($IrMn_4$) nanocrystals exhibit nontrivial electronic band structures, which may contribute to the observed intriguing AHE in the $Ir_{20}Mn_{80}$ film. Obvious anisotropic and negative parallel magnetoresistances were also observed in the $Ir_{20}Mn_{80}$, which is consistent with the possible non-trivial topology of the electronic band structures. Moreover, the electrical switching of the antiferromagnetic $Ir_{20}Mn_{80}$ has been implemented by the spin Hall current from adjacent Pt layer. All these results impart the magnetron-sputtered $Ir_{20}Mn_{80}$ a great potential for the future antiferromagnetic spintronics applications.

2. Results and discussion

Thin films of $Ir_{20}Mn_{80}$ (6)/MgO (2.5)/Ta (3), $Ir_{20}Mn_{80}$ (6)/CoFeB (5)/MgO (2.5)/Ta (3), and Pt (5)/$Ir_{20}Mn_{80}$ (6)/MgO (2.5)/Ta (3) were deposited on thermally oxidized Si substrates by using magnetron sputtering, where the thicknesses in the parentheses are in nanometers. The sample $Ir_{20}Mn_{80}$ (6)/CoFeB (5)/MgO (2.5)/Ta (3) was annealed at 250 °C under an in-plane magnetic field 1 T for 1 hour to obtain the exchange bias. For electrical transport measurements, Hall bar and star-shape devices were fabricated by standard photolithography and dry etching techniques (see Fig. S1 in supporting information). Figure 1(a) shows the M–H curves of the sample holder with or without the $Ir_{20}Mn_{80}$ sample, and the net magnetization extracted for the $Ir_{20}Mn_{80}$ film is negligible small ($\sim$ 2 emu/cc) as shown in the inset of Fig. 1(a), which is in consistence with the antiferromagnetic character of the $Ir_{20}Mn_{80}$. Then the in-plane magneto optical Kerr effect was measured for the $Ir_{20}Mn_{80}$/CoFeB sample as shown in the Fig. 1(b). Obvious exchange bias effect can be observed with an exchange bias field of $\sim$ 36.2 mT, which verifies the $Ir_{20}Mn_{80}$ being AFM with strong exchange coupling to the CoFeB.

Hall measurements were conducted for the Hall bar device of the $Ir_{20}Mn_{80}$ sample at different temperatures. Figure 1(c) shows the perpendicular magnetic field ($\mu_0 H_z$) dependence of the transverse resistance ($R_{\rm Hall}$) with the magnetic field up to 9 T and the temperatures from 10 K to 400 K. As can be observed, the AHE is remarkable at all the temperatures for the $Ir_{20}Mn_{80}$ sample. The AHE is traditionally considered to exist in ferromagnetic metals with broken time-reversal symmetry and strong spin–orbit coupling, and thus is proportional to the magnetization. The result here is rather intriguing since the magnetism of the $Ir_{20}Mn_{80}$ is negligible small as shown in Fig. 1(a). Moreover, the magnetic field dependent behavior and the saturation magnetic field are different for the AHE resistance in Fig. 1(c) and the magnetism in Fig. 1(a). All these results suggest that the AHE observed in the sputtered $Ir_{20}Mn_{80}$ may have an origin other than that of the common AHE in ferromagnets.

From Fig. 1(c), the AHE of the $Ir_{20}Mn_{80}$ can also be found to have a strong temperature dependence, and the anomalous Hall resistance increases with increasing the temperature from 10 K to 150 K, then decreases with further increasing the temperature. We calculated the anomalous Hall conductivity (AHC) $\sigma_{\rm AHE}$ of the $Ir_{20}Mn_{80}$ by the equation of $\sigma_{\rm AHE} \approx -\rho_{xy}/\rho^2$, where ρ_{xy} is the anomalous Hall resistivity and ρ is the longitudinal zero-field resistivity, and the results were plotted in Fig. 1(d). As can be observed, the $\sigma_{\rm AHE}$ increases from 3.6 $\Omega^{-1}\cdot{\rm cm}^{-1}$ to 7.9 $\Omega^{-1}\cdot{\rm cm}^{-1}$ with increasing the temperature from 10 K to 150 K, then decreases to 0.5 $\Omega^{-1}\cdot{\rm cm}^{-1}$ with further increasing the temperature to 400 K. Similar temperature dependence of the AHE has also been reported in the non-collinear AFMs such as Mn_3Ge and Mn_3Sn,[23,56] which was related with the evolution of the non-trivial electronic band structure with temperature.[12]

Apart from the AHE, non-trivial electronic band structures of non-collinear AFMs such as Mn_3Sn and Mn_3Ge have also been reported to induce unique magnetotransport behavior.[13,22,56] The magnetoresistance could strongly depend on the angle between the external magnetic field and the current, and the magnetoresistance is negative when the current is parallel to the magnetic field. Figure 2(b) presents the measured magnetoresistance curves at 10 K with different angles between the current and the magnetic field as schematized in Fig. 2(a). Remarkably, the magnetoresistance is strongly dependent on the angle between the current and the magnetic field, and negative parallel magnetoresistance up to $\sim$ 0.03% can be observed when the magnetic field is parallel to the current. The magnetoresistance involves into positive values when the magnetic field is tilted to the film normal direction. Moreover, the negative parallel magnetoresistance is robust at high magnetic field up to 9 T.

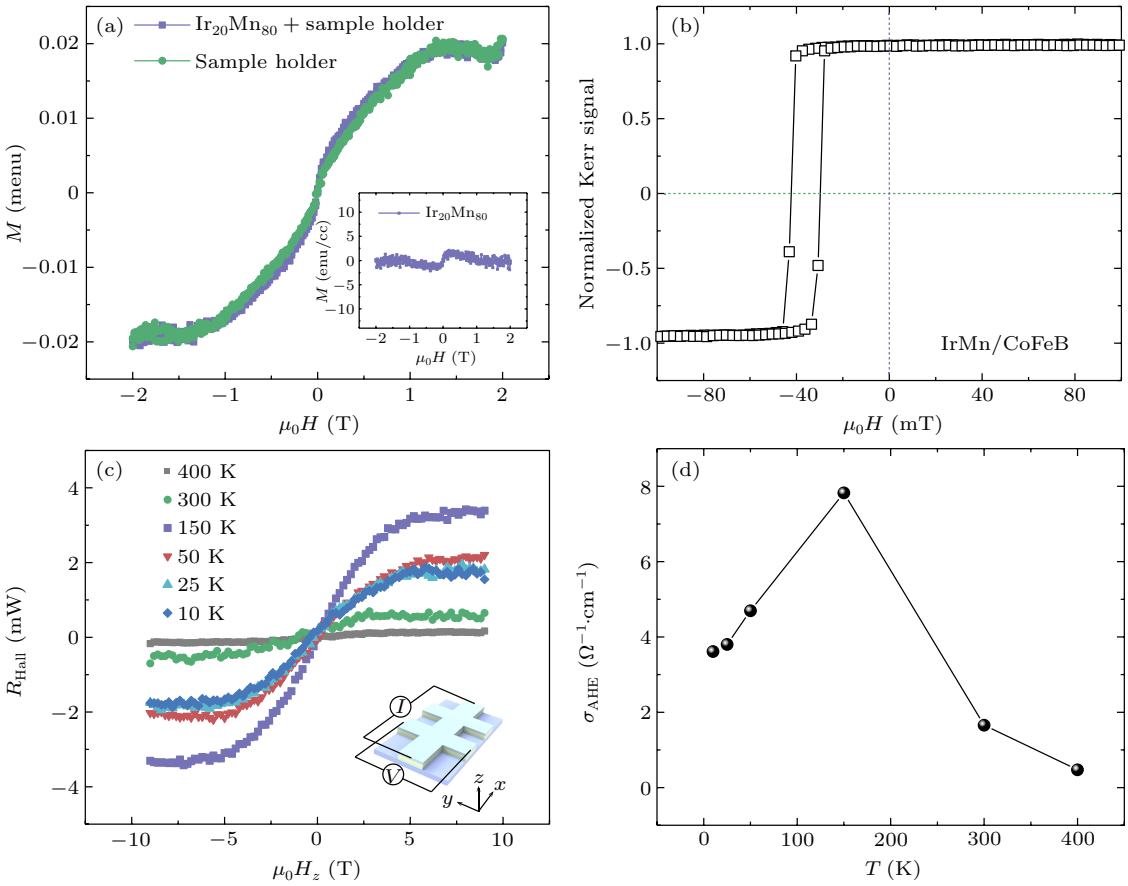


Fig. 1. (a) The magnetic hysteresis loop of the $Ir_{20}Mn_{80}$ film with sample holder (purple squares), and the reference signal of the sample holder without sample (green circles). The insert represents the extracted magnetic signal of the $Ir_{20}Mn_{80}$ film. (b) The magnetic hysteresis loop of the $Ir_{20}Mn_{80}$/CoFeB sample. (c) Anomalous Hall effect of the $Ir_{20}Mn_{80}$ under the perpendicular magnetic field at different temperatures. Inset: Sketch of the Hall measurement geometry. (d) Anomalous Hall conductivity as a function of the temperature.

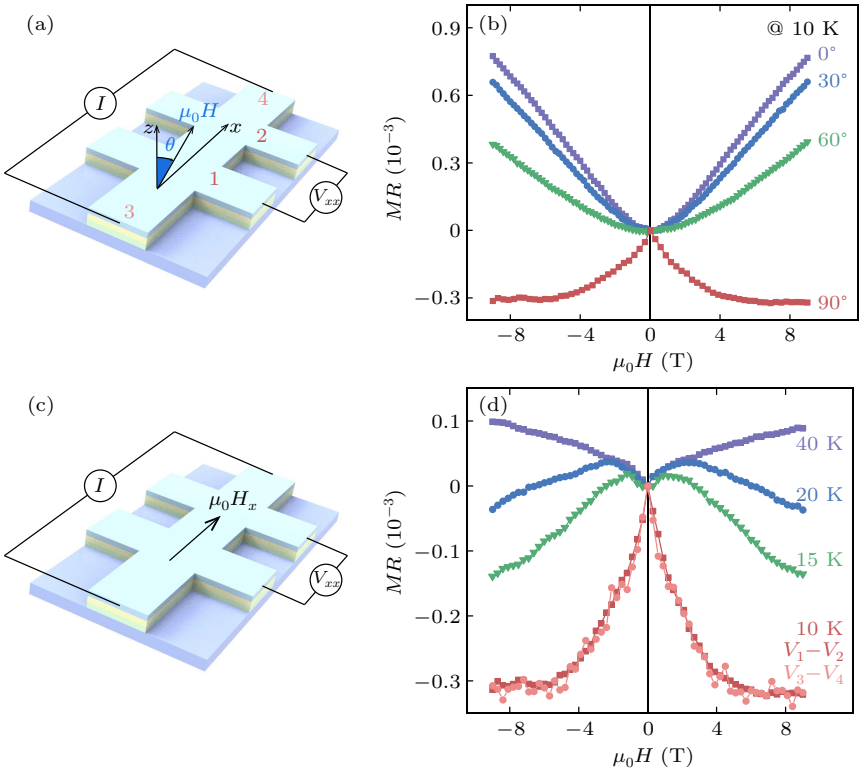


Fig. 2. (a) The schematic diagram of the measurement geometry for anisotropy magnetoresistance. (b) The magnetoresistance with different angles between the current and the magnetic field at 10 K. (c) The schematic diagram of the measurement geometry for the magnetoresistance with the magnetic field parallel to the current. (d) The magnetoresistance at different temperatures with the magnetic field parallel to the current.

Figure 2(d) shows the magnetoresistance measured at different temperatures from 10 K to 40 K with the magnetic field fixed parallel to the electrical current as schematized in Fig. 2(c). As a result, the negative magnetoresistance is suppressed by increasing the temperature and ultimately disappears above 40 K. The temperature dependence of the negative magnetoresistance excludes the origin of the magnetic field-induced suppression of magnetic fluctuations which decreases with decreasing the temperature.[22] In contrast, the negative magnetoresistance matches with the non-trivial band origin, which would be enhanced with decreasing the temperature due to the reduced inelastic scattering effects at low temperatures.[22] Another extrinsic mechanism that may yield negative magnetoresistance is the current-jetting effect due to the non-uniform current distribution inside the sample.[57] To check this possibility, we employed two pairs of voltage terminals, V_1–V_2 and V_3–V_4, as shown in Fig. 2(a). Figure 2(d) displays the magnetoresistance curves detected by the two pairs of probes, which show almost the same results, ruling out the possible current-jetting effect. The observed anisotropic and negative parallel magnetoresistance are in line with the reported topological magnetotransport in non-collinear AFMs such as Mn_3Sn and Mn_3Ge.[13,56] Therefore, the anisotropic and negative parallel magnetoresistance in the $Ir_{20}Mn_{80}$ may arise due to the non-trivial electronic band structures.

Previous theoretical works have predicted a large AHC in the non-collinear antiferromagnetic Mn_3Ir, where the AHE arises from an intrinsic nonzero Berry curvature due to the Kagome configuration of the Mn atoms and strong spin–orbit coupling.[17] Recent experiments have confirmed the prominent AHE in the Mn_3Ir despite the measured AHC value is smaller than the predicted values.[58] The $Ir_{20}Mn_{80}$ has the atomic ratio close to that of the Mn_3Ir. Thus, we build an artificial Ir_4Mn_{16} ($IrMn_4$) crystal based on the structure of Mn_3Ir, and calculated the electronic band structures and the AHC of the artificial Ir_4Mn_{16} ($IrMn_4$) crystal. The artificial $Ir_{20}Mn_{80}$ ($IrMn_4$) crystal was built by repeating the crystal of Mn_3Ir five times along z axis and substituting one Ir atom with one Mn atom, which produced the Ir_4Mn_{16} ($IrMn_4$) crystal to mimic the $Ir_{20}Mn_{80}$. The calculation is based on the Vienna *ab-initio* simulation package and the Kubo formula approach following the previous reports[15,59] (see Fig. S2 in supporting information).

Figure 3 shows the calculated electronic band structure and the energy-dependent AHC element of σ_{yz} for the Mn_3Ir and Ir_4Mn_{16} ($IrMn_4$) crystals. For comparison, as shown in Figs. 3(a) and 3(b), the electronic band structure and AHC for the Mn_3Ir crystal are calculated and the results are consistent with the previous reports.[15,18] It is noted that the Mn_3Ir was reported to exhibit a strong peak of the band sum of the Berry curvature at momentum points where spin–orbit coupling lifts the degeneracies,[15,18] such as at the R point in Fig. 3(a). The electronic band structure of Ir_4Mn_{16} ($IrMn_4$) shows topological properties similar to that of Mn_3Ir, especially around the M and R points as shown in Fig. 3(c). And due to the crystal structure repetition and high proportion of Mn element, more band state splitting occurs in Ir_4Mn_{16} ($IrMn_4$), which may contribute to the slightly higher AHC value (190 $\Omega^{-1}\cdot cm^{-1}$) at the Fermi level than that (185 $\Omega^{-1}\cdot cm^{-1}$) of Mn_3Ir as shown in Figs. 3(b) and 3(d), although the AHC trends of both Mn_3Ir and Ir_4Mn_{16} ($IrMn_4$) with the change of energy are consistent. The transmission electron microscopy measurement has been performed for the $Ir_{20}Mn_{80}$ film, which indicates that the $Ir_{20}Mn_{80}$ is generally amorphous but may have local nanocrystalline structures (see Fig. S3 in supporting information). In this sense, the AHE observed in the $Ir_{20}Mn_{80}$ film may arise due to the topological electronic band structures of the Ir_4Mn_{16} ($IrMn_4$) nanocrystals. On the other hand, the Mn atoms are known easy to diffuse in thin film stacks, and the electron energy loss spectroscopy results indicate that the Mn spreads wider and diffuses more to the MgO layer than the Ir (see Fig. S3 in supporting information). A reduced Mn/Ir ratio in the $Ir_{20}Mn_{80}$ film can be expected in some regions. Therefore, the possible presence of both Ir_4Mn_{16} ($IrMn_4$) and Mn_3Ir nanocrystals may contribute to the AHE observed in $Ir_{20}Mn_{80}$ films. Previous work indicated that the polycrystalline $Ir_{20}Mn_{80}$ films could be formed by grains of Mn_3Ir and stabilized in Mn_3Ir spin structures.[55,60] Based on this, $Ir_{20}Mn_{80}$, under an applied magnetic field, could have oriented grains[61] and exhibit macroscopic AHE signals as shown in Fig. 1(c). From this point of view, the latter explanation based on Mn_3Ir nanocrystals is favored but this still requires further theoretical and experimental efforts.

To demonstrate the electrical switching of the antiferromagnetic $Ir_{20}Mn_{80}$, we employed the heavy metal Pt as the spin current source, and measured the change of the anisotropic magnetoresistance (AMR) and/or spin Hall magnetoresistance (SMR) in Pt/$Ir_{20}Mn_{80}$ to detect the magnetization switching of AFM Néel vector.[62] Since both AMR and SMR are even in magnetization, *i.e.*, it is invariant upon magnetization reversal,[63] the Pt/$Ir_{20}Mn_{80}$ film was patterned to the star-shape devices as shown in Fig. 4(a), and orthogonal currents were applied to induce 90° switching of $Ir_{20}Mn_{80}$ Néel vector to maximize the AMR and/or SMR signal. Following the procedures to study the electrical switching of antiferromagnets such as CuMnAs,[64] Mn_2Au,[31] and MnN,[62] the electrical current writing of $Ir_{20}Mn_{80}$ was achieved by applying pulse currents with width of 100 μs (write 1 and write 2) along two orthogonal directions, and the corresponding transverse Hall resistance (R_{Hall}) was measured with a dc current (I_{probe}) of 0.5 mA that was much smaller than the writing pulses. After each "write 1" pulse, the R_{Hall} was measured with a delay of 2 s, and the relaxation of R_{Hall} was then monitored over 80 s after 20 "write 1" pulses were applied. Subsequently, same measurements were executed after the "write 2" pulse. A complete switching cycle thus consisted of three re-

peats of 20 pulses per current direction and relaxation phases of 80 s. The measured $R_{\rm Hall}$ results corresponding to each writing pulse and relaxation phase are shown in the Fig. 4(b). Notably, a periodic change in $R_{\rm Hall}$ can be observed, and the $R_{\rm Hall}$ changes oppositely after applying orthogonal writing current pulses. The $R_{\rm Hall}$ switching traces of the Pt/$Ir_{20}Mn_{80}$ have similar features as those of the SOT-induced switching of the CuMnAs,[64] Mn_2Au,[31] and MnN.[62]

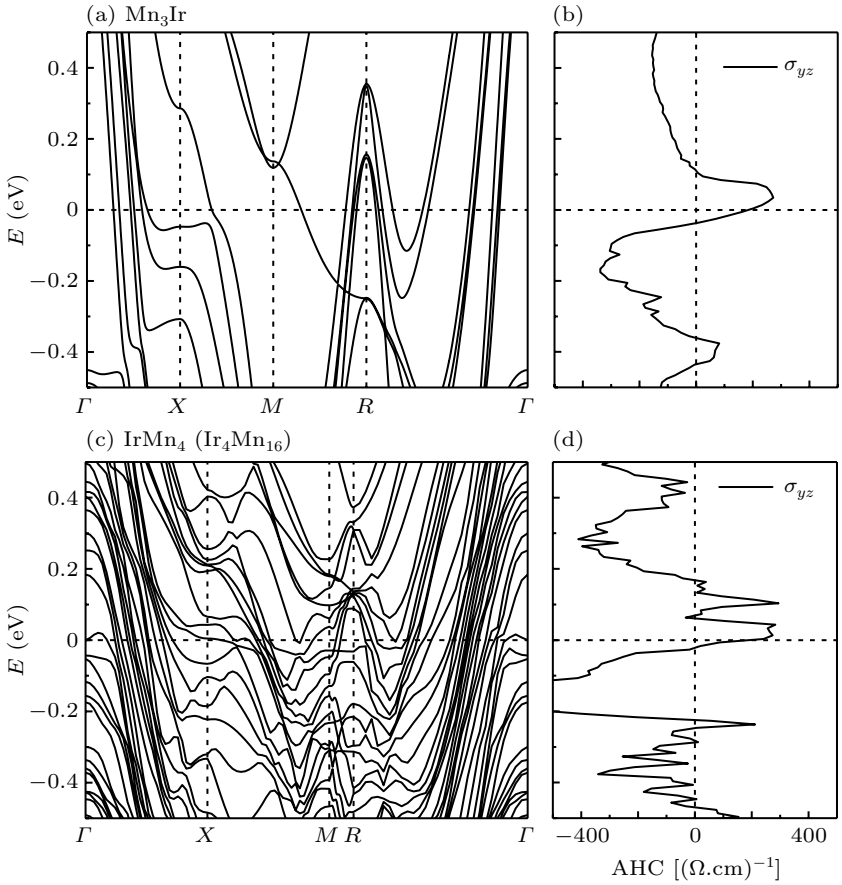


Fig. 3. (a) Electronic band structure for the Mn_3Ir. (b) Energy-dependent AHC element of σ_{yz} for the Mn_3Ir. (c) Electronic band structure for the Ir_4Mn_{16} ($IrMn_4$). (d) Energy-dependent AHC element of σ_{yz} for the Ir_4Mn_{16} ($IrMn_4$).

A few recent works have related the "saw-tooth" shape of transverse voltage with the resistive contribution which arise due to the thermal degradation of Pt in the electrical switching experiments, either by the heating induced local crystallization or by the electromigration.[39,41] Dunz *et al.* have carefully investigated the resistive contribution in the electrical switching of MnN,[62] and found that the resistive contribution only arises with applying $j_{\rm Pt} \geq 11 \times 10^{11}$ A·m^{-2}. During our experiments, the current density flowing in Pt is no more than 6.25×10^{11} A·m^{-2}. Thus, the resistive contribution is probably not the dominant source of the observed electrical $R_{\rm Hall}$ switching in the Pt/$Ir_{20}Mn_{80}$. We further measured the $R_{\rm Hall}$ switching traces under an external magnetic field of 3 T along x direction, and the results indicate that the periodic $R_{\rm Hall}$ switching traces disappear with the applied magnetic field (see Fig. S4 in supporting information). This result suggests a magnetic origin of the periodic $R_{\rm Hall}$ switching in the Pt/$Ir_{20}Mn_{80}$ structure. The 3-T magnetic field is high enough to align the magnetic order as revealed by the AHE results in Fig. 1(c) and the planar Hall effect (PHE) results in Fig. S4, and thus hinders the electrical switching of the magnetic order of the $Ir_{20}Mn_{80}$.

To facilitate a quantitative analysis of the $R_{\rm Hall}$ switching results, we utilized the analysis method from previous work.[62] The switching traces are separated into two regimes, *i.e.*, the pulsing and relaxation phases, as shown in Fig. 4(c). The data in the pulsing regime are fitted by the function

$$R_{\rm p}(n) = c_0 + c_1 \exp(-n/\lambda) + c_2 n,$$

where $c_{0,1,2}$ and λ are fitting parameters and n is the pulse number. The fitting produces the absolute switching amplitude $|\Delta R_{\rm a}|$ which is the difference of the $R_{\rm Hall}$ before and after applying the pulse current along one current line. The relaxation regime, consisting of the relaxation of an ensemble of grains which have a range of relaxation times, could be modeled by a stretched exponential decay of $R_{\rm r}(t) = d_0 + d_1 \exp(-\alpha t^{\beta})$, where $d_{0,1}$, α, and β are fitting parameters. Based on the fitting results, the anisotropy energy barrier $E_{\rm B}$ can be obtained using the equations of $\tau_{\rm s} = (1/\alpha)^{1/\beta}$, $\langle\tau\rangle = (\tau_{\rm s}/\beta)\Gamma(1/\beta)$, and $\tau = f_0^{-1} \exp(E_{\rm B}/k_{\rm B}T)$, where $\Gamma(x)$ is the gamma function, $f_0 \approx 10^{12}$ s^{-1} is the attempt frequency,[62,65] $k_{\rm B}$ is the

Boltzmann constant, and T is the absolute temperature. As can be observed in Fig. 4(c), both the pulsing and relaxation phases of the R_{Hall} results can be well fitted, and the resulting $|\Delta R_{\mathrm{a}}|$ and E_{B} with different pulse current densities were shown in the Fig. 4(d). The $|\Delta R_{\mathrm{a}}|$ increases with increasing the writing current density, while the E_{B} does not change much at different current densities, which is similar to the results of the SOT-induced switching of the antiferromagnetic MnN.[62] The characteristic analyses of the electrical switching results of the $Ir_{20}Mn_{80}$ are well in consistence with the thermal activation scenario of the SOT-driven antiferromagnet switching.[64] For the read-out mechanism, we propose the AHE and PHE originating from the $Ir_{20}Mn_{80}$ layer or the spin Hall magnetoresistance (SMR) originating from the Pt layer may be responsible. A detailed study of the AHE, PHE, and SMR is necessary to gain further insight into the dominant read-out mechanism. The present electrical switching of the antiferromagnetic $Ir_{20}Mn_{80}$ renders a great potential of the sputtered $Ir_{20}Mn_{80}$ for high thermal stability antiferromagnetic spintronics compatible with the existing complementary metal–oxide–semiconductor technology.

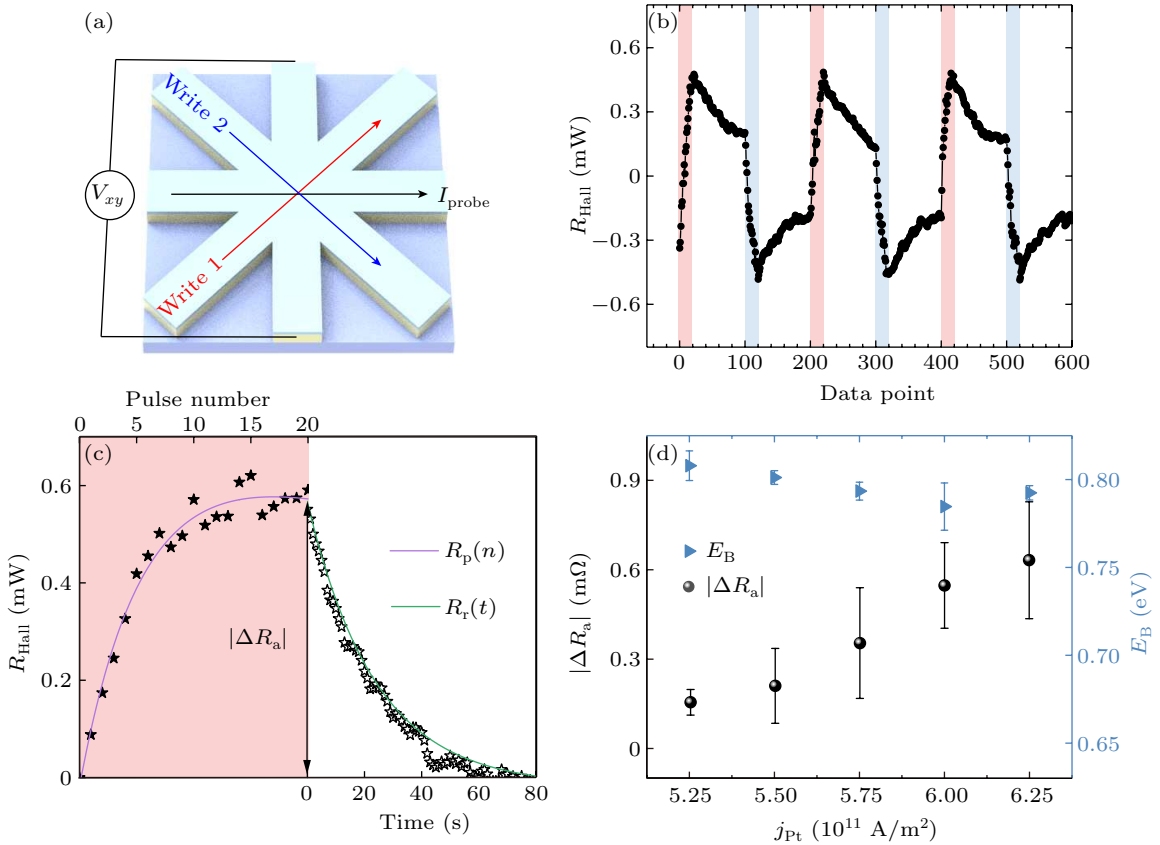


Fig. 4. (a) Schematic diagram of the measurement geometry for electrical switching. The red and blue arrows represent the current pulse directions. (b) Electrical switching and relaxation signals. The background colors correspond to applying pulses along the two pulse lines (red, blue) or the relaxation phase (white). (c) Exemplary fitting procedure for the pulsing and relaxation phases. $|\Delta R_{\mathrm{a}}|$ represents the absolute switching amplitude. (d) Pulse current density dependence of the absolute switching amplitude $|\Delta R_{\mathrm{a}}|$ and the switching energy barrier E_{B}. The results are averaged over three devices and the error bars correspond to the standard deviation.

3. Conclusion

In summary, we have observed remarkable AHE in the magnetron-sputtered antiferromagnetic $Ir_{20}Mn_{80}$. The *ab initio* calculations indicate the topological electronic band structures of Ir_4Mn_{16} ($IrMn_4$) nanocrystals may contribute the observed AHE in the sputtered $Ir_{20}Mn_{80}$ film. The $Ir_{20}Mn_{80}$ also shows anisotropic and negative parallel magnetoresistance, which is in consistence with the non-trivial electronic band structures. Moreover, we demonstrated the current-induced switching of the antiferromagnetic $Ir_{20}Mn_{80}$ in the $Pt/Ir_{20}Mn_{80}$ metallic bilayer. The characteristics of the switching are well consistent with the thermal activation model of the SOT-driven antiferromagnet switching. The presented results endow the magnetron-sputtered $Ir_{20}Mn_{80}$ a good platform for exploring the topological antiferromagnet-based spintronics applications.

Supplementary material

See the supplementary material for details on sample and devices fabrication, measurement, *ab-initio* simulation method, structure characterizations, element distribution analysis, and the electrical switching of $Ir_{20}Mn_{80}$ under 3-T magnetic field.

Acknowledgments

The authors thank Shujun Hu for helpful discussions. Project supported by the Tencent Foundation through the XPLORER PRIZE, the National Key Research and Development Program of China (Grant Nos. 2018YFB0407602 and 2021YFB3601303), and the National Natural Science Foundation of China (Grant Nos. 61627813, 11904017, 92164206, and 61571023).

References

[1] Jungwirth T, Marti X, Wadley P and Wunderlich J 2016 *Nat. Nanotechnol.* **11** 231
[2] Khymyn R, Lisenkov I, Tiberkevich V, Ivanov B A and Slavin A 2017 *Sci. Rep.* **7** 43705
[3] Kosub T, Kopte M, Hühne R, Appel P, Shields B, Maletinsky P, Hühner R, Liedke M O, Fassbender J, Schmidt O G and Makarov D 2017 *Nat. Commun.* **8** 13985
[4] Olejník K, Seifert T, Kašpar Z, *et al.* 2018 *Sci. Adv.* **4** eaar3566
[5] Lopez-Dominguez V, Almasi H and Amiri P K 2019 *Phys. Rev. Appl.* **11** 024019
[6] Olejník K, Schuler V, Marti X, Novák V, Kašpar Z, Wadley P, Campion R P, Edmonds K W, Gallagher B L, Garces J, Baumgartner M, Gambardella P and Jungwirth T 2017 *Nat. Commun.* **8** 15434
[7] Wang Y, Zhu D, Yang Y, Lee K, Mishra R, Go G, Oh S H, Kim D H, Cai K, Liu E, Pollard S D, Shi S, Lee J, Teo K L, Wu Y, Lee K J and Yang H 2019 *Science* **366** 1125
[8] Ross A, Lebrun R, Gomonay O, Grave D A, Kay A, Baldrati L, Becker S, Qaiumzadeh A, Ulloa C, Jakob G, Kronast F, Sinova J, Duine R, Brataas A, Rothschild A and Kläui M 2020 *Nano Lett.* **20** 306
[9] Li J, Wilson C B, Cheng R, Lohmann M, Kavand M, Yuan W, Aldosary M, Agladze N, Wei P, Sherwin M S and Shi J 2020 *Nature* **578** 70
[10] Vaidya P, Morley S A, van Tol J, Liu Y, Cheng R, Brataas A, Lederman D and del Barco E 2020 *Science* **368** 160
[11] Zhu D, Zhang T, Fu X, Hao R, Hamzić A, Yang H, Zhang X, Zhang H, Du A, Xiong D, Shi K, Yan S, Zhang S, Fert A and Zhao W 2022 *Phys. Rev. Lett.* **128** 217702
[12] Nakatsuji S, Kiyohara N and Higo T 2015 *Nature* **527** 212
[13] Kuroda K, Tomita T, Suzuki M T, *et al.* 2017 *Nat. Mater.* **16** 1090
[14] Higo T, Man H, Gopman D B, *et al.* 2018 *Nat. Photon.* **12** 73
[15] Zhang Y, Sun Y, Yang H, Železný J, Parkin S P P, Felser C and Yan B 2017 *Phys. Rev. B* **95** 075128
[16] Kimata M, Chen H, Kondou K, Sugimoto S, Muduli P K, Ikhlas M, Omori Y, Tomita T, MacDonald A H, Nakatsuji S and Otani Y 2019 *Nature* **565** 627
[17] Nayak A K, Fischer J E, Sun Y, Yan B, Karel J, Komarek A C, Shekhar C, Kumar N, Schnelle W, Kübler J, Felser C and Parkin S S P 2016 *Sci. Adv.* **2** e1501870
[18] Chen H, Niu Q and MacDonald A H 2014 *Phys. Rev. Lett.* **112** 017205
[19] Kübler J and Felser C 2014 *Europhys. Lett.* **108** 67001
[20] Yang H, Sun Y, Zhang Y, Shi W J, Parkin S S P and Yan B 2017 *New J. Phys.* **19** 015008
[21] Ikhlas M, Tomita T, Koretsune T, Suzuki M T, Nishio-Hamane D, Arita R, Otani Y and Nakatsuji S 2017 *Nat. Phys.* **13** 1085
[22] Tsai H, Higo T, Kondou K, *et al.* 2020 *Nature* **580** 608
[23] Higo T, Qu D, Li Y, Chien C L, Otani Y and Nakatsuji S 2018 *Appl. Phys. Lett.* **113** 202402
[24] Mukherjee J, Suraj T S, Basumatary H, Sethupathi K and Raman K V 2021 *Phys. Rev. Mater.* **5** 014201
[25] Chen H, Feng Z, Yan H, Qin P, Zhou X, Guo H, Wang X, Wu H, Zhang X, Meng Z and Liu Z 2021 *Phys. Rev. B* **104** 064428
[26] Wadley P, Howells B, Železný J, *et al.* 2016 *Science* **351** 587
[27] Grzybowski M J, Wadley P, Edmonds K W, Beardsley R, Hills V, Campion R P, Gallagher B L, Chauhan J S, Novak V, Jungwirth T, Maccherozzi F and Dhesi S S 2017 *Phys. Rev. Lett.* **118** 057701
[28] Godinho J, Reichlová H, Kriegner D, *et al.* 2018 *Nat. Commun.* **9** 4686
[29] Bodnar S Y, Šmejkal L, Turek I, Jungwirth T, Gomonay O, Sinova J, Sapozhnik A A, Elmers H J, Kläui M and Jourdan M 2018 *Nat. Commun.* **9** 348
[30] Zhou X F, Chen X Z, Zhang J, Li F, Shi G Y, Sun Y M, Saleem M S, You Y F, Pan F and Song C 2019 *Phys. Rev. Appl.* **11** 054030
[31] Meinert M, Graulich D and Matalla-Wagner T 2018 *Phys. Rev. Appl.* **9** 064040
[32] Železný J, Gao H, Výborný K, Zemen J, Mašek J, Manchon A, Wunderlich J, Sinova J and Jungwirth T 2014 *Phys. Rev. Lett.* **113** 157201
[33] Zelezný J, Gao H, Manchon A, Freimuth F, Mokrousov Y, Zemen J, Mašek J, Sinova J and Jungwirth T 2017 *Phys. Rev. B* **95** 014403
[34] Moriyama T, Oda K, Ohkochi T, Kimata M and Ono T 2018 *Sci. Rep.* **8** 14167
[35] Baldrati L, Gomonay O, Ross A, *et al.* 2019 *Phys. Rev. Lett.* **123** 177201
[36] Schreiber F, Baldrati L, Schmitt C, Ramos R, Saitoh E, Lebrun R and Kläui M 2020 *Appl. Phys. Lett.* **117** 082401
[37] Baldrati L, Schmitt C, Gomonay O, Lebrun R, Ramos R, Saitoh E, Sinova J and Kläui M 2020 *Phys. Rev. Lett.* **125** 077201
[38] Cheng Y, Yu S, Zhu M, Hwang J and Yang F 2020 *Phys. Rev. Lett.* **124** 027202
[39] Zhang P, Finley J, Safi T and Liu L 2019 *Phys. Rev. Lett.* **123** 247206
[40] Cogulu E, Statuto N N, Cheng Y, Yang F, Chopdekar R V, Ohldag H and Kent A D 2021 *Phys. Rev. B* **103** L100405
[41] Chiang C C, Huang S Y, Qu D, Wu P H and Chien C L 2019 *Phys. Rev. Lett.* **123** 227203
[42] Meer H, Schreiber F, Schmitt C, Ramos R, Saitoh E, Gomonay O, Sinova J, Baldrati L and Kläui M 2021 *Nano Lett.* **21** 114
[43] Takeuchi Y, Yamane Y, Yoon J Y, Itoh R, Jinnai B, Kanai S, Ieda J i, Fukami S and Ohno H 2021 *Nat. Mater.* **20** 1364
[44] Higo T, Kondou K, Nomoto T, Shiga M, Sakamoto S, Chen X, Nishio-Hamane D, Arita R, Otani Y, Miwa S and Nakatsuji S 2022 *Nature* **607** 474
[45] Deng Y, Liu X, Chen Y, Du Z, Jiang N, Shen C, Zhang E, Zheng H, Lu H Z and Wang K 2022 *Natl. Sci. Rev.* **10** nwac154
[46] DuttaGupta S, Kurenkov A, Tretiakov O A, Krishnaswamy G, Sala G, Krizakova V, Maccherozzi F, Dhesi S S, Gambardella P, Fukami S and Ohno H 2020 *Nat. Commun.* **11** 5715
[47] Shi J, Lopez-Dominguez V, Garesci F, Wang C, Almasi H, Grayson M, Finocchio G and Khalili Amiri P 2020 *Nat. Electron.* **3** 92
[48] Guo Z, Yin J, Bai Y, Zhu D, Shi K, Wang G, Cao K and Zhao W 2021 *Proc. IEEE* **109** 1398
[49] Stobiecki T, Kanak J, Wrona J, Czapkiewicz M, Kim C G, Kim C O, Tsunoda M and Takahashi M 2004 *Phys. Status Solidi A* **201** 1621
[50] Markou A, Taylor J M, Kalache A, Werner P, Parkin S S P and Felser C 2018 *Phys. Rev. Mater.* **2** 051001
[51] Qian J F, Nayak A K, Kreiner G, Schnelle W and Felser C 2014 *J. Phys. D: Appl. Phys.* **47** 305001
[52] Rinaldi C, Baldrati L, Loreto M D, Asa M, Bertacco R and Cantoni M 2018 *IEEE Trans. Magn.* **54** 1
[53] Hoshino K, Nakatani R, Hoshiya H, Sugita Y and Tsunashima S 1996 *Jpn. J. Appl. Phys.* **35** 607
[54] Fuke H N, Saito K, Kamiguchi Y, Iwasaki H and Sahashi M 1997 *J. Appl. Phys.* **81** 4004
[55] Kohn A, Kovács A, Fan R, McIntyre G J, Ward R C C and Goff J P 2013 *Sci. Rep.* **3** 2412
[56] Qin P, Feng Z, Zhou X, Guo H, Wang J, Yan H, Wang X, Chen H, Zhang X, Wu H, Zhu Z and Liu Z 2020 *ACS Nano* **14** 6242
[57] Hu J, Rosenbaum T F and Betts J B 2005 *Phys. Rev. Lett.* **95** 186603
[58] Iwaki H, Kimata M, Ikebuchi T, Kobayashi Y, Oda K, Shiota Y, Ono T and Moriyama T 2020 *Appl. Phys. Lett.* **116** 022408
[59] Qiao J, Zhou J, Yuan Z and Zhao W 2018 *Phys. Rev. B* **98** 214402
[60] Yamaoka T 1974 *J. Phys. Soc. Jpn.* **36** 445
[61] Mendes J B S, Cunha R O, Alves Santos O, Ribeiro P R T, Machado F L A, Rodríguez-Suárez R L, Azevedo A and Rezende S M 2014 *Phys. Rev. B* **89** 140406
[62] Dunz M, Matalla-Wagner T and Meinert M 2020 *Phys. Rev. Res.* **2** 013347
[63] Baltz V, Manchon A, Tsoi M, Moriyama T, Ono T and Tserkovnyak Y 2018 *Rev. Mod. Phys.* **90** 015005
[64] Matalla-Wagner T, Rath M F, Graulich D, Schmalhorst J M, Reiss G and Meinert M 2019 *Phys. Rev. Appl.* **12** 064003
[65] Vallejo-Fernandez G, Aley N P, Chapman J N and O'Grady K 2010 *Appl. Phys. Lett.* **97** 222505